

Generation of a Mn(IV)–Peroxo or Mn(III)–Oxo–Mn(III) Species upon Oxygenation of Mono- and Binuclear Thiolate-Ligated Mn(II) Complexes

Chien-Ming Lee,^{*,†} Wun-Yan Wu,[†] Ming-Hsi Chiang,^{*,‡} D. Scott Bohle,^{*,§} and Gene-Hsiang Lee^{||}

[†]Department of Applied Science, National Taitung University, Taitung 950, Taiwan

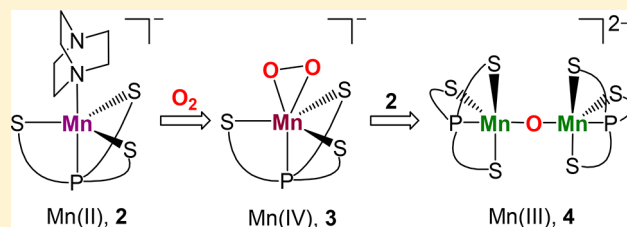
[‡]Institute of Chemistry, Academia Sinica, Taipei 115, Taiwan

[§]Department of Chemistry, McGill University, Montreal, Quebec H3A 0B8, Canada

^{||}Instrumentation Center, National Taiwan University, Taipei 107, Taiwan

Supporting Information

ABSTRACT: A thiolate-bridged binuclear complex $[\text{PPN}]_2[(\text{Mn}^{\text{II}}(\text{TMSPS}_3))_2]$ (**1**, PPN = bis(triphenylphosphine)-iminium and $\text{TMSPS}_3 = (2,2',2''\text{-trimercapto-3,3',3''-tris(trimethylsilyl)triphenylphosphine)}$), prepared from the reaction of $\text{MnCl}_2/[\text{PPN}]\text{Cl}$ and $\text{Li}_3[\text{TMSPS}_3]$, converts into a mononuclear complex $[\text{PPN}][\text{Mn}^{\text{II}}(\text{TMSPS}_3)(\text{DABCO})]$ (**2**) in the presence of excess amounts of DABCO (DABCO = 1,4-diazabicyclo[2.2.2]octane). Variable temperature studies of solution containing **1** and DABCO by UV–vis spectroscopy indicate that **1** and **2** exist in significant amounts in equilibrium and mononuclear **2** is favored at low temperature. Treatment of **1** or **2** with the monomeric O_2 -side-on-bound $[\text{PPN}][\text{Mn}^{\text{IV}}(\text{O}_2)(\text{TMSPS}_3)]$ (**3**) produces the mono-oxo-bridged dimer $[\text{PPN}]_2[(\text{Mn}^{\text{III}}(\text{TMSPS}_3))_2(\mu\text{-O})]$ (**4**). The electrochemistry of **1** and **2** reveals anodic peak(s) for a $\text{Mn}^{\text{III}}/\text{Mn}^{\text{II}}$ redox couple at shifted potentials against Fc/Fc^+ , indicating that both complexes can be oxidized by dioxygen. The O_2 activation mediated by **1** and **2** is investigated in both solution and the solid state. Microcrystals of **2** rapidly react with air or dry O_2 to generate the Mn(IV)–peroxo **3** in high yield, revealing a solid-to-solid transformation and two-electron reduction of O_2 . Oxygenation of **1** or **2** in solution, however, is affected by diffusion and transient concentration of dioxygen in the two different substrates, leading to generation of **3** and **4** in variable ratios.

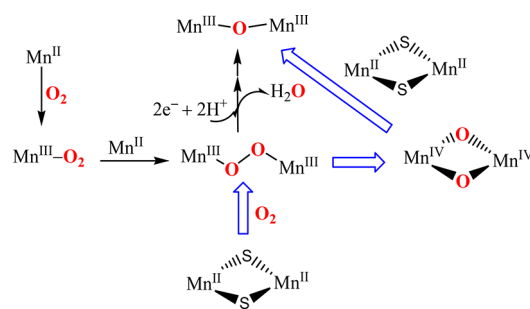


INTRODUCTION

Coordination compounds with Mn–peroxo moieties have attracted considerable attention,^{1–21} due to their varied roles in key biological processes which include the activation of molecular oxygen,^{22–25} detoxification of superoxide and hydrogen peroxide,^{26–29} and water-splitting chemistry.^{30–32} The metastable Mn–peroxo intermediates that undergo O–O bond cleavage produce high-valent Mn–oxo adducts which are responsible for substrate oxidation and are also of interest in biological^{33,34} and synthetic chemistry.^{16,35–39} In this regard, understanding the mechanisms of Mn-mediated dioxygen activation remains a significant challenge. Based on the key intermediates such as metal–superoxo, –peroxo, –hydroperoxo, or –oxo obtained in enzymatic and biomimetic systems (metal = iron or copper), a potential mechanism for metal-promoted dioxygen activation has been established.⁴⁰ Compared to the Fe^{39–41} and Cu-mediated^{42–44} dioxygen chemistry, the reported chemistry relative to Mn-mediated activation of O_2 is scarce.^{2,5,16,19–21,37,39} Recently reported examples of mononuclear and binuclear Mn^{II} –thiolate complexes include one by Kovacs et al. which shows that a series of five-coordinate mononuclear thiolate-coordinated Mn(II) complexes can react with O_2 .^{12,14,18,21} Here, more

than one intermediate is involved (black arrows in Scheme 1), but the reaction includes a structurally characterized peroxo-bridged binuclear Mn(III) complex which slowly converts to the mono-oxo-bridged binuclear Mn(III) species.¹⁴ This example also reveals that the thiolate ligand is capable of stabilizing metal–peroxo species. Very recently, oxygenation of a dimercapto-bridged Mn^{II} –thiolate dimer reported by Duboc¹⁴

Scheme 1

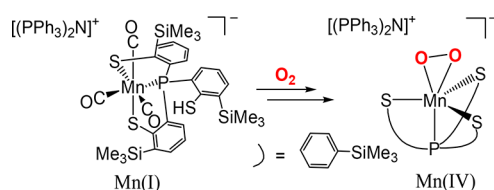


Received: June 14, 2017

group resulted in the isolation of a di- μ -oxo Mn(IV) dimer that may be generated following homolytic O–O bond cleavage of peroxy-bridged binuclear Mn(III) species (blue arrows in Scheme 1).²¹ In this system, additional Mn^{II}–thiolate dimer is required to convert the di- μ -oxo Mn(IV) dimer to mono-oxo-bridged binuclear Mn(III) species (via a comproportionation reaction).

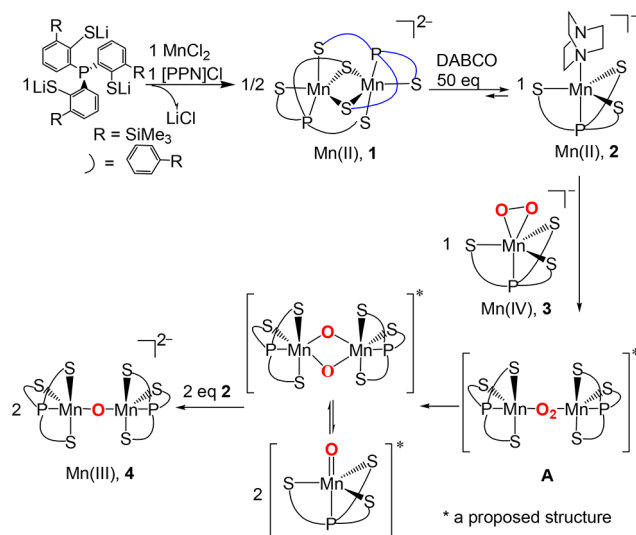
Treatment of transition-metal–thiolate complexes with O₂ frequently causes ligand-centered oxidation, resulting in the formation of metal–sulfenate, –sulfinate, or –sulfonate species.^{45–48} On the other hand, coordination of chelating ligands containing strongly donating thiolato sulfur(s) is found to help metal-based O₂ activation by lowering the metal redox potential.^{16,18,21,49} Thiolates with noninnocent character also serve as good chelators to help stabilize high-valent complexes. One example of this class is the tetradentate-deprotonated TMS⁺PS³⁻ ligand which contains three thiolates and phosphine.^{50–55} In previous studies, we have demonstrated that treatment of a thiolate-ligated Mn(I) complex containing a pendant thiol group with O₂ can generate a monomeric O₂-side-on-bound [PPN][Mn^{IV}(TMS⁺PS³⁻)(O₂)] which is metastable in organic solvent and stable in the solid state at ambient temperature (Scheme 2).⁵⁵ The activation of O₂ is proposed to

Scheme 2



go through a four-coordinated [Mn^{II}(TMS⁺PS³⁻)]⁻ intermediate. In this work, we report the synthesis of mononuclear and binuclear thiolate-ligated Mn(II) complexes, [PPN]₂[(Mn^{II}(TMS⁺PS³⁻))₂] (**1**) and [PPN][Mn^{II}(TMS⁺PS³⁻)(DABCO)] (**2**), by utilizing MnCl₂ as Mn(II) ion source (Scheme 3). Reaction of **1** and **2** with different oxidants e.g., [PPN][Mn^{IV}(TMS⁺PS³⁻)(O₂)] (**3**) and O₂, has been investigated

Scheme 3



in solution and in the solid state, leading to solid-to-solid direct oxygenation of **2** by O₂.

RESULTS AND DISCUSSION

Preparation of Binuclear 1, Mononuclear 2, and Mono-Oxo-Bridged Dimeric 4. When a THF solution of deprotonated TMS⁺PS³⁻ ligand (as a trilitium salt) is added to a CH₃CN solution of MnCl₂/[PPN]Cl mixture in a 1:1:1 molar ratio, an immediate change in solution color from light yellow to orange red is observed. The reaction mixture leads to the isolation of dimeric [PPN]₂[(Mn^{II}(TMS⁺PS³⁻))₂] (**1**, 95% yield) after recrystallization from vapor diffusion of Et₂O into CH₃CN solution of **1** under N₂ at room temperature (Scheme 3). The optical spectrum of **1** in CH₃CN solution is featureless at wavelengths above 550 nm (Figure 1). Upon addition of

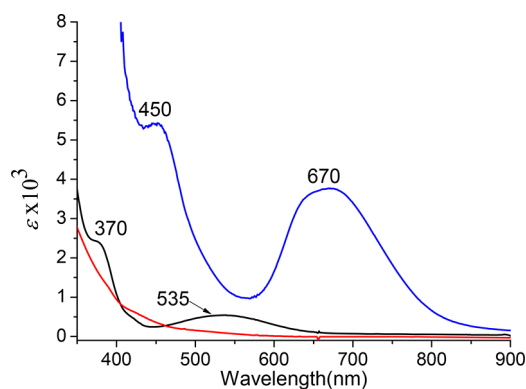


Figure 1. UV–vis spectra (in CH₃CN) for **1** (red line), **2** (black line), and **4** (blue line) at room temperature (ϵ , M⁻¹ cm⁻¹).

excess amounts of DABCO (100 equiv) into a CH₃CN solution of **1**, the resulting mixture immediately turns purple. The change is also observed in the UV–vis spectrum in which a 535 nm absorption band is responsible for purple color of DABCO adduct (Figure 1). In titration experiments, as observed by UV–vis spectroscopy (Figure 1S), ~50 equiv of DABCO is needed to maximize the growth of the peak at 535 nm. Dark purple crystals of a DABCO adduct suitable for X-ray crystallography are obtained by slowly adding the diethyl ether to layer above the mixture (90% yield). Characterization by X-ray crystallography revealed the purple DABCO adduct to be a five-coordinate monomeric [PPN][Mn^{II}(TMS⁺PS³⁻)(DABCO)] (**2**).

Upon treatment of peroxomanganese(IV) **3**⁵⁵ with **2** in CH₃CN at ambient temperature under N₂, a green adduct with absorption bands at 450 ($\epsilon = 5410$) and 670 ($\epsilon = 3760$) nm is immediately formed. Dark green crystals obtained by vapor diffusion of Et₂O into CH₃CN solution and characterized by X-ray crystallography reveal the green adduct to be a mono-oxo-bridged dimeric [PPN]₂[(Mn^{III}(TMS⁺PS³⁻))₂(μ -O)] (**4**) (95% yield, Scheme 3).

Molecular Structures of Complexes 1, 2, and 4. ORTEP diagrams of anions **1**, **2**, and **4** are presented in Figures 2–4 with selected bond distances and angles being given in the figure captions. The two Mn sites of **1** are crystallographically equivalent, and the two [Mn₂S₂] cores appear as a coplanar diamond shape with a zero dihedral angle crystallographically imposed between the S1MnS1A and S1MnAS1A planes. The distance between two Mn(II) ions is 3.0055(13) Å, which is too long for a direct metal–metal

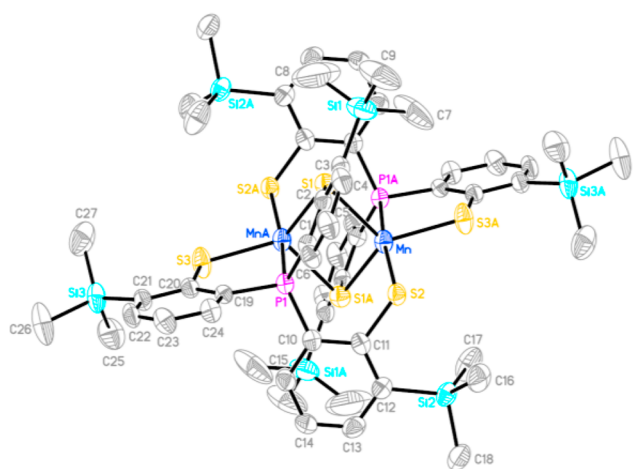


Figure 2. ORTEP diagrams of dianion **1** with thermal ellipsoids drawn at the 50% probability level. Hydrogen atoms and solvent of crystallization are omitted for clarity. Selected bond distances (Å) and angles (deg): Mn–S1 2.5438(14); Mn–S2 2.4627(13); Mn–S1A 2.5045(14); Mn–S3A 2.4254(14); Mn–P1A 2.6140(13); S1–Mn–S2 102.57(4); S1–Mn–S3A 119.08(5); S1–Mn–S1A 106.93(4); S1–Mn–P1A 88.80(4); S2–Mn–S1A 97.08(5); S2–Mn–S3A 94.62(5); S2–Mn–P1A 168.50(5); S1A–Mn–S3A 128.41(5); S1A–Mn–P1A 77.71(4); S3A–Mn–P1A 81.06(4); Mn–S1–MnA 73.07(4).

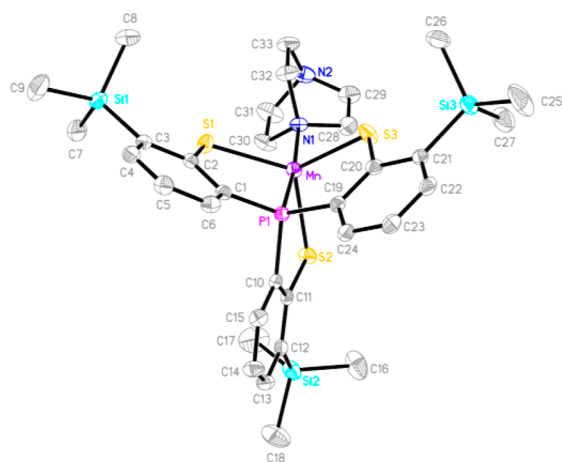


Figure 3. ORTEP diagrams of anion **2** with thermal ellipsoids drawn at the 50% probability level. Hydrogen atoms and solvent of crystallization are omitted for clarity. Selected bond distances (Å) and angles (deg): Mn–S1 2.5295(8); Mn–S2 2.4987(8); Mn–S3 2.5041(9); Mn–N1 2.226(2); Mn–P1 2.4429(8); S1–Mn–S2 117.67(3); S1–Mn–S3 121.44(3); S2–Mn–S3 112.94(3); S1–Mn–N1 94.77(7); S1–Mn–P1 79.47(3); S2–Mn–N1 105.41(6); S2–Mn–P1 80.96(3); S3–Mn–N1 98.54(6); S3–Mn–P1 81.31(3); N1–Mn–P1 172.99(7).

interaction. The geometry about both central Mn(II) can be regarded as distorted trigonal bipyramidal ($\tau = 0.67$) with three thiolates located in equatorial positions and the phosphorus occupying an axial position trans to the fourth thiolato sulfur. The average Mn–S_{bridge} and Mn–S_{terminal} bond lengths of **1** are 2.5242(14) and 2.4441(13) Å, respectively, which are comparable to those of [Mn^{II}₂(LS)(LSH)]ClO₄ (LS = 2,2'-(2,2'-bipyridine-6,6'-diyl)bis(1,1-diphenylethanethiolate)).¹⁸ The geometry of anion **2** ($\tau = 0.86$) exhibits closer to the ideal trigonal bipyramidal than that of **1** with three thiolates located in equatorial positions and the phosphorus occupying an axial position trans to DABCO. The mean Mn(II)–SR bond

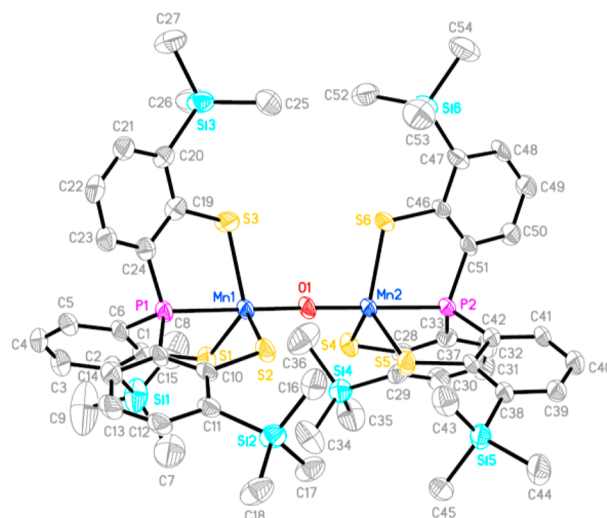


Figure 4. ORTEP diagrams of dianion **4** with thermal ellipsoids drawn at the 50% probability level. Hydrogen atoms and solvent of crystallization are omitted for clarity. Selected bond distances (Å) and angles (deg): Mn1–S1 2.4031(19); Mn1–S2 2.3779(18); Mn1–S3 2.3861(18); Mn1–P1 2.3208(17); Mn1–O1 1.774(3); Mn2–S4 2.3553(19); Mn2–S5 2.3938(17); Mn2–S6 2.3738(17); Mn2–P2 2.3328(16); Mn2–O1 1.775(3); S1–Mn1–S2 116.58(7); S1–Mn1–S3 116.19(7); S2–Mn1–S3 120.57(7); O1–Mn1–P1 177.79(14); O1–Mn2–P2 178.54(14).

distance of **2** (2.5108(9)) is longer than that of five-coordinate mononuclear thiolate-coordinated [Mn^{II}(S^{Me}₂N₄(6-Me-DPEN)](BF₄)⁺ (6-Me-DPEN = *N,N*-bis(6-methyl-2-pyridylmethyl)ethane-1,2-diamine)¹² It can be attributed to rich charge density on the Mn(II) center, provided by three thiolate donors, reducing the interaction between Mn ion and thiolato sulfurs. The geometry around both central Mn(III) in **4** adopt trigonal bipyramidal geometry ($\tau = 0.95$) with three thiolates located in equatorial positions and the phosphorus occupying an axial position trans to the bridged-oxo ligand. The distances of Mn1–O1 and Mn2–O2 are nearly identical, and the Mn1...Mn2 separation is 3.548 Å, both of which are comparable with other examples containing a single, unsupported oxo-bridged Mn(III) dimer.^{12,56–62} The mean Mn(III)–SR bond distance of **4** (2.390(2) Å) is longer than those of unsupported oxo-bridged Mn(III)–thiolate dimers (range from 2.255 to 2.297 Å),¹² and dinuclear [Mn^{III}₂(edt)₄]^{2–} (Mn–S_{terminal} = 2.32 Å, edt = 1,2-ethanedithiolate)⁶³ and [Mn₂(Im)(edt)₄][–] (the mean Mn–S = 2.335 Å, Im[–] = anion imidazole).⁶⁴ The shorter mean Mn–SR bond distance of **4** than that of **1** or **2** is indicative of an increase in oxidation state of Mn from Mn(II) to Mn(III).

Magnetic Properties of Complexes **1**, **2**, and **4**.

Magnetic susceptibility (χ_M) of microcrystalline samples of **1**, **2**, and **4** is measured under an external field of 2000 G, respectively. The χ_M value of **1** decreases from 0.0114 cm³ mol^{–1} at 300 K to a minima of 2.339 × 10^{–3} cm³ mol^{–1} at 12 K and increases to 4.253 × 10^{–3} cm³ mol^{–1} at 2 K (Figure 5a). The corresponding $\chi_M T$ value of **1** between 300 and 2 K decreases from 3.4109 to 8.256 × 10^{–3} cm³ mol^{–1} K. The value at 300 K for **1** is significantly deviated from the theoretical value of 8.75 cm³ mol^{–1} K for a system composed of two non-interacting high-spin Mn^{II} centers ($S = 5/2$, $g = 2$). This suggests that a strong antiferromagnetic interaction is present between the Mn centers of **1**. The $\chi_M T$ data is fitted to an

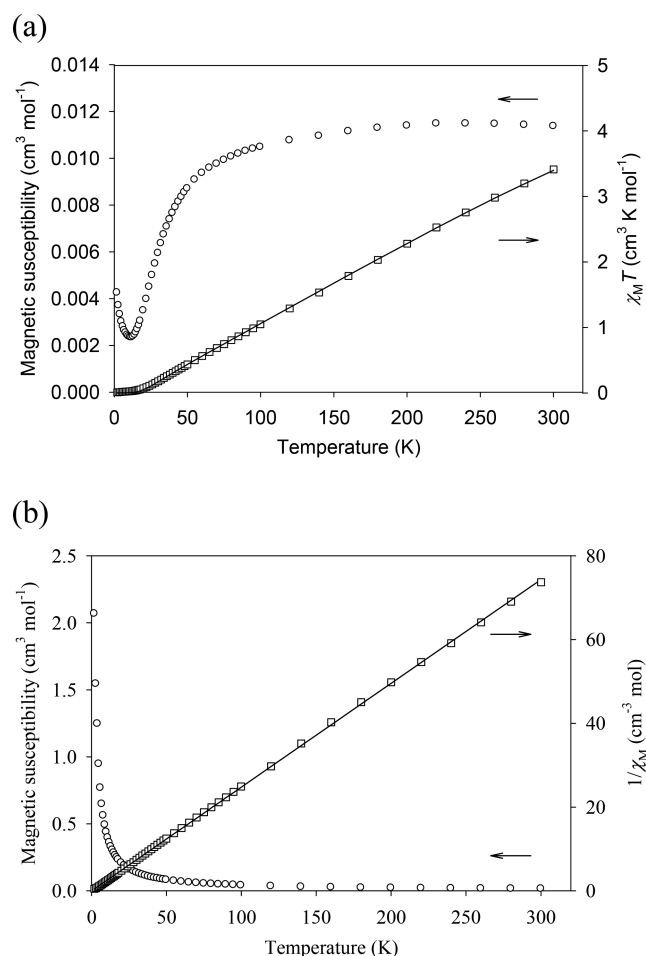


Figure 5. (a) Plots of χ_M (open circles) and $\chi_M T$ (open squares) versus temperature for **1**. The solid line is the best fit of the experimental data to the theoretical expression. (b) Plots of χ_M (open circles) and $1/\chi_M$ (open squares) versus temperature for **2**. The solid line is the best fit of the experimental data to the Curie–Weiss law.

expression of $H = -2J \cdot S_1 \cdot S_2$ ($S_1 = S_2 = 5/2$) in which $2J$ represents the magnetic exchange parameter. A satisfactory fit is obtained: $g = 1.991(9)$, $2J = -57.0(5)$ cm⁻¹, which is comparable to that of $[\text{Mn}^{\text{II}}_2(\text{LS})(\text{LSH})]\text{ClO}_4$ ($J = -22(1)$ cm⁻¹),¹⁸ revealing that the high-spin Mn^{II} ions of **1** are strongly antiferromagnetically coupled.

As shown in Figure 5b, the χ_M value of microcrystalline samples of **2** increases from 0.0136 cm³ mol⁻¹ at 300 K to 2.0667 cm³ mol⁻¹ at 2 K. The corresponding inverse χ_M value of **2** displays a linear relationship against temperature, indicating the Curie–Weiss paramagnetic behavior for a $S = 5/2$ spin ground state system ($C = 4.04$ cm³ K mol⁻¹, $\theta = 0.1436$ K). The results from the magnetic investigation suggests a high-spin Mn^{II} center in **2**.¹²

The χ_M value of mono-oxo-bridged dimeric $[\text{PPN}]_2[(\text{Mn}^{\text{III}}(\text{TMSPS3}))_2(\mu\text{-O})]$ (**4**) gradually decreases from 4.451×10^{-3} cm³ mol⁻¹ at 300 K to 3.017×10^{-3} cm³ mol⁻¹ at 50 K and then increases to 0.011 cm³ mol⁻¹ at 2 K (Figure S2). The corresponding $\chi_M T$ value between 300 and 2 K decreases from 1.335 to 0.022 cm³ mol⁻¹ K. The value at 300 K is significantly deviated from the theoretical value of 6 cm³ mol⁻¹ K for a system composed of two non-interacting high-spin Mn^{III} centers ($S = 2$, $g = 2$). Thus, a strong antiferromagnetic interaction is present between the Mn

centers via an oxo bridge, consistent with the observation that an oxo group is a good spin mediator.⁶⁵ The $\chi_M T$ data is fitted to an expression of $H = -2J \cdot S_1 \cdot S_2$ ($S_1 = S_2 = 2$) in which $2J$ represents the magnetic exchange parameter. A satisfactory fit is obtained between 100 and 300 K: $g = 2.01(3)$, $2J = -152(3)$ cm⁻¹, which falls into the range of known mono-oxo-bridged Mn(III) dimers^{12,58–62,66} and reveals that the high-spin Mn^{III} ions of **4** are strongly antiferromagnetically coupled.

Electrochemical and EPR Spectra of Complexes 1 and 2. The electrochemical behavior of **1** (1.0 mM) measured by cyclic voltammetry (CV) in CH₃CN with 0.1 M $[n\text{-Bu}_4\text{N}][\text{PF}_6]$ as supporting electrolyte, under N₂, reveals two successive and reversible redox processes at $E_{1/2} = -1.10$ V and $E_{1/2} = -0.77$ V, respectively (vs Fc/Fc⁺). The electrochemistry of **2** shows only one reversible redox process at $E_{1/2} = -1.16$ V against Fc/Fc⁺ (Figure 6). In comparison with redox

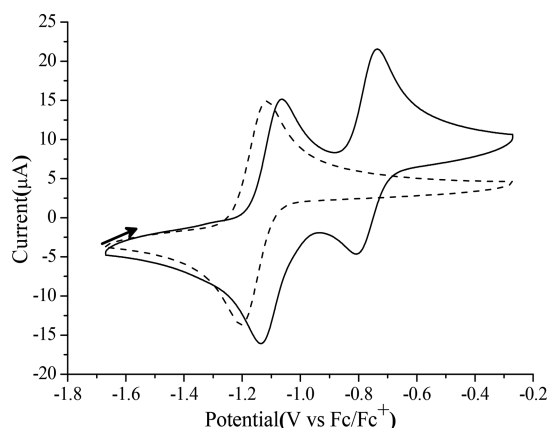


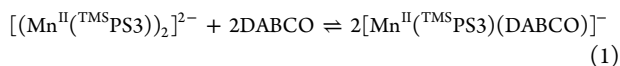
Figure 6. Cyclic voltammograms of **1** (solid line) and **2** (dashed line) measured in a 1 mM CH₃CN solution with 0.1 M $[n\text{-Bu}_4\text{N}][\text{PF}_6]$ as the supporting electrolyte at room temperature, scan rate 0.1 V/s. $E_{1/2} = -1.16$ V ($E_p = 89$ mV) for **2**; $E_{1/2} = -1.10$ V ($E_p = 70$ mV) and $E_{1/2} = -0.77$ V ($E_p = 73$ mV) for **1**.

properties of Li₃^{TMS}PS3 (Figure S3), ligand-centered redox processes of **1** and **2** can be ruled out.^{67–69} The event at -1.10 V can be assigned to a Mn^{III}Mn^{II}/Mn^{II}Mn^{II} redox couple, and the electrochemically generated Mn^{II}Mn^{III} species can be further oxidized to Mn^{III}Mn^{III} at -0.77 V. The reversible redox process at $E_{1/2} = -1.16$ V of **2** is assigned to the Mn^{III}/Mn^{II} redox couple. Within the CH₃CN solvent window, no redox wave is observed for the Mn^{IV}/Mn^{III} couple of **1** and **2**.^{55,70} A dimercapto-bridged dimer $[\text{Mn}^{\text{II}}_2(\text{LS})(\text{LSH})]\text{ClO}_4$ with a pendant thiol group (its CV has an irreversible anodic peak at -0.01 V vs Fc/Fc⁺) and the deprotonated form $[\text{Mn}^{\text{II}}_2(\text{LS})_2]$ which shows a reversible peak at -0.45 V vs Fc/Fc⁺ have been recently reported.^{18,21} The assignment of these redox events as a pair of one-electron oxidations for Mn^{II}Mn^{II} to Mn^{III}Mn^{III} couple reveals different electrochemical behavior from that of **1**. The drop in potential of **1** may be attributed to coordinated ^{TMS}PS3³⁻ ligand that contains three thiolates with better donor ability than thiol to place the Mn(II) ion in an electron-rich condition. The electrochemical stability of a mixed-valence Mn^{II}/Mn^{III} species of **1** can be attributed to relatively rigid tetradentate ligand and the redox noninnocence of ^{TMS}PS3³⁻.^{67,68} Those factors also lend the support to the explanation of more negative potential of mononuclear **2** compared to other monomeric thiolate-ligated Mn(II) complexes such as $[\text{Mn}^{\text{II}}(\text{S}^{\text{Me}2}\text{N}_4(6\text{-Me-DPEN}))](\text{BF}_4)^+$ with

a reversible $\text{Mn}^{\text{III/II}}$ redox couple at $E_{1/2} = 0.41$ V (vs SCE; 0.035 V vs Fc/Fc⁺).¹² Moreover, the lower potentials associated with the $\text{Mn}^{\text{III/II}}$ redox couple indicate that **1** and **2** are much easier to oxidize by an oxidant such as O_2 .

Although the CVs of **1** and **2** indicate that the solid-state structure of dimeric **1** is mostly retained in CH_3CN (a weaker donor than DABCO), the partial dissociation of **1** in CH_3CN to form mononuclear solvent-bound $[\text{Mn}^{\text{II}}(\text{TMS}^{\text{PS}}\text{3})(\text{NCCH}_3)]^-$ is not ruled out. The X-band EPR spectrum of mononuclear **2** recorded at 77 K displays an intense broad signal at $g_{\perp} = 5.21$ and a less intense signal at $g_{\parallel} = 1.95$ (Figure S4), again consistent with an axial high-spin Mn^{II} center in **2**. It is noted that the 77 K EPR spectrum of dimeric **1** in CH_3CN shows very weak signals, the g -values of which are similar to those of **2** (Figure S4). In the solid state, **1** shows strong antiferromagnetic interaction between two $\text{Mn}(\text{II})$ centers, suggesting that the EPR spectrum of **1** could be silent at low temperature. The resonance signals observed by EPR of **1** in CH_3CN may be attributed to mononuclear solvent-bound $[\text{Mn}^{\text{II}}(\text{TMS}^{\text{PS}}\text{3})(\text{NCCH}_3)]^-$ species. Similarly, very weak peaks are observed in the ESI-MS (electrospray ionization mass spectrum) at $m/z = 667.2$ ($[\text{Mn}^{\text{II}}(\text{TMS}^{\text{PS}}\text{3})(\text{NCCH}_3)]^-$, $m/z = 667.1$ (calcd); Figure S5).

Van't Hoff Plot for Conversion of 1 to 2. Variable temperature studies of solutions containing **1** and excess amounts of DABCO by UV-vis spectroscopy indicate that **1** and **2** exist in significant amounts in equilibrium. Based on the equilibrium manner in eq 1, the equilibrium constant (K_{eq}) is 9(1) at 25 °C, which is comparable to the K_{eq} observed between $[\text{Cu}^{\text{III}}(\text{TMS}^{\text{PS}}\text{3})(\text{Cl})]^-$ and $\text{Cu}^{\text{III}}(\text{TMS}^{\text{PS}}\text{3})(\text{DABCO})$ in CH_3CN .⁵¹ An analysis of the Van't Hoff plot from 298 to 248 K for this reaction displays the activation parameters $\Delta H^\circ = -16(1)$ kJ mol⁻¹, $\Delta S^\circ = -37(2)$ J K⁻¹ mol⁻¹, indicating that the monomeric **2** is favored at low temperature (Figure 7).



Oxidation of 1 or 2 with Mn(IV)-Peroxo Species.⁵⁵ In titration experiments, as observed by UV-vis spectroscopy (Figure 8), ~3.0 equiv of mononuclear **2** is needed to fully transform **3** into **4** and the formation of **4** is nearly quantitative based on the amount of peroxomanganese(IV) **3** (eq 2).

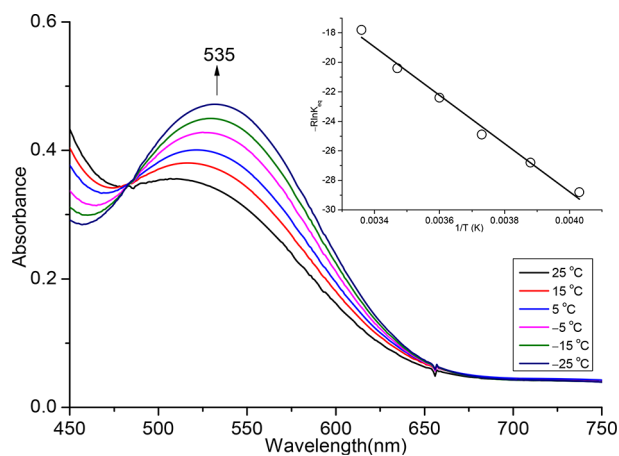


Figure 7. Changes of UV-vis spectra of CH_3CN solution containing **1** (0.60 mM) and DABCO (13.8 mM) observed from 25 to -25 °C. Inset: Van't Hoff plot of equilibrium data based on eq 1.

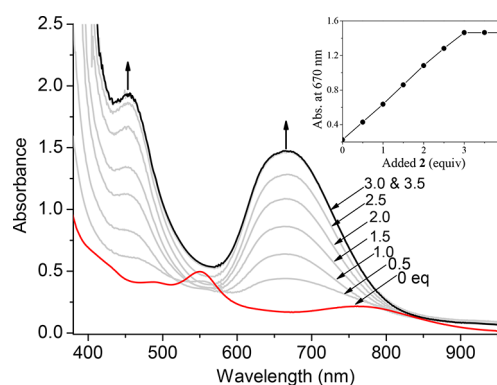
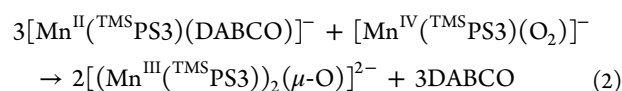


Figure 8. UV-vis spectra of complexes **3** (red) and **4** (black), respectively. Changes in UV-vis spectra (gray) after treating **3** with various equivalents of **2** in CH_3CN at room temperature. Inset: absorbance changes at 670 nm upon addition of **2**.



Recently, a mono-oxo-bridged $\{[\text{Mn}^{\text{III}}(\text{S}^{\text{Me}}\text{2N}_4(6\text{-Me- DPEN}))_2(\mu\text{-O})]^{2+}$ reported by Kovacs's group was generated from the thermal decomposition of metastable peroxo-bridged $\{[\text{Mn}^{\text{III}}(\text{S}^{\text{Me}}\text{2N}_4(6\text{-Me- DPEN}))_2(\text{trans-}\mu\text{-1,2-O}_2)]^{2+}$.¹⁴ The mechanism for the formation this binuclear $\text{Mn}(\text{III})$ -peroxo species has been demonstrated to involve a mononuclear $\text{Mn}(\text{III})$ -superoxo intermediate that reacts with the second equivalent of $[\text{Mn}^{\text{II}}(\text{S}^{\text{Me}}\text{2N}_4(6\text{-Me- DPEN}))]^+$ (black arrows in Scheme 1).¹⁶ By analogy with widely accepted pathways to explain the formation of μ -peroxo and -oxo dimetallic species,^{16,39-41} we propose that mononuclear $\text{Mn}(\text{II})$ **2** reacts with peroxomanganese(IV) **3** to yield a binuclear $[(\text{TMS}^{\text{PS}}\text{3})\text{-Mn}^{\text{III}}(\mu\text{-O}_2^{2-})\text{-Mn}^{\text{III}}(\text{TMS}^{\text{PS}}\text{3})]^{2-}$ (intermediate **A**, Scheme 3). Low-temperature UV-vis spectroscopy is utilized to detect the peroxo-to-manganese charge transfer band which has been observed at higher energy visible region,^{8,16} but no intermediates are observed upon mixing **2** and **3** in $\text{CH}_3\text{CH}_2\text{CN}$ at -70 °C. In related systems, peroxo-bridged dimanganese intermediates have been observed and their stability has been attributed to ligand intramolecular interactions, including aromatic ring π -stacking, which stabilize these reactive species.¹⁴

It is noted that stoichiometric quantities for this reaction are three equiv of **2** per equiv of **3** (eq 2). An independent experiment shows that **2** can react with iodobenzene (PhIO ; 0.5 equiv), an oxygen-atom transfer reagent, to produce **4** in nearly quantitative yield. These observations suggest that the formation of **4** involves a high-valent Mn -oxo transient species that, in the case of O_2 addition, would be generated from O-O bond cleavage in **A** (Scheme 3).¹² Then, the generated Mn -oxo species reacts rapidly with **2** (2 equiv) to form 2 equiv of μ -oxo dimeric **4**.^{21,39,41} Therefore, the total consumption for **2** is 3 equiv, which is consistent with the titration experiments.

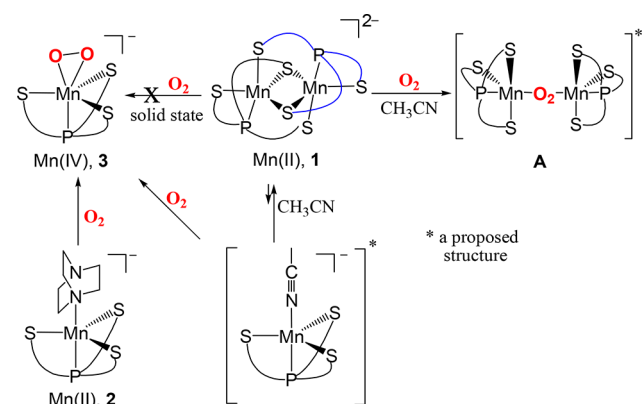
In a competition experiment of **2** with triphenylphosphine (PPh_3) for oxygen atom transfer mediated by Mn -oxo species we observe that the yield of **4** is unperturbed based on UV-vis spectroscopy when reacting **2** and **3** in the presence of excess amounts of PPh_3 . The formation of OPPh_3 is not observed in this reaction presumably due to the fast reaction between Mn -oxo transient species and mononuclear **2**. This observation also suggests that intermediary complexes do not have electrophilic

oxygens and that they are thus relatively electron rich. Binuclear **1** also reacts with **3** to generate **4**, but the yield of **4** from this reaction is decreased to 75% based on the absorbance peaks at 670 ($\epsilon = 3760$) of **4** (Figure S6).

Oxidation of **1** and **2** with Dioxygen, Respectively.

Complex **2** is highly reactive with dioxygen both in solution and in the solid state. Since the oxidation of **2** with O_2 in solution is more complicated, we discuss the reaction in the solid state first. Microcrystals of **2** are placed under air or dry O_2 at ambient temperature for 2 h. The color change during oxidation of solid-state **2** with O_2 is subtle, from light purple to dark red-purple (Figure S7). The UV-vis spectrum of solid-to-solid oxygenation product dissolved in CH_3CN under N_2 atmosphere shows three features at 490, 550, and 755 nm, indicating the formation of peroxomanganese(IV) **3** (Scheme 4; 95% yield based on the ϵ value at 550 nm).⁷¹ The peak at

Scheme 4



903 cm^{-1} (ν_{OO}) is observed after microcrystals of **2** are stood in open air at ambient temperature for 2 h (Figure S8), which is consistent with the formation of **3** in the solid state. When $^{18}O_2$ is used during solid-state oxygenation of **2**, we observe the shift of ν_{OO} to lower energy ($\sim 861\text{ cm}^{-1}$, Figure S8), confirming that O_2 is the source of peroxo ligand in **3**.⁵⁵ However, lattice parameters recorded for single-crystal **2** before and after exposure to air for 30 min at room temperature are the same. This observation may indicate that solid-state oxygenation of **2** occurs on the surface of particles. Prolonged exposure of microcrystals of **2** to air leads to a loss of crystallinity of **2** that is confirmed by powder X-ray diffraction (Figure S9). The presence or absence of solvent like *n*-hexane in the solid state does not affect dioxygen binding to **2**. No re-formation of **2** upon prolonged evacuation of **3** is observed at room temperature, indicating that the binding of O_2 to **2** is irreversible.

In CH_3CN solution, treatment of **2** with excess O_2 at ambient temperature results in the formation of mixed products as evidenced by UV-vis spectroscopy (Figure 9). Calculations from spectral deconvolution revealed that **3** (63%) and **4** (8%) are responsible for this pattern (Figure S10). As shown in Figure 9, the ratio between generated **3** and **4** in this reaction depends upon the transient oxygen concentration.²¹ For example, the yield of **3** increases when the solution is purged with a vigorous stream of O_2 into the solution of **2**, and the yield is higher than that when gas O_2 is layered above the solution (Figure S11). Given these observations, a sequence of isolated products after mixing O_2 with **2** is peroxomanganese-

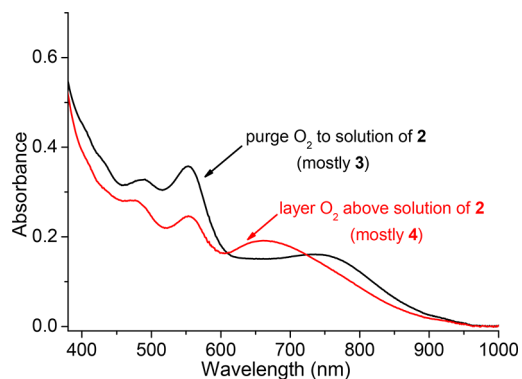


Figure 9. Comparisons of UV-vis spectra between purging O_2 into and layering O_2 above CH_3CN solution of **2** (0.2 mM).

(IV) **3** first in solution as well as in the solid state (Scheme 4). This can be rationalized as follows: in solution, the diffusion rate of **2** is fast enough to react with **3** and vice versa to produce **4**, which is consistent with a separate study of the reaction **2** with **3** (Scheme 3). However, in the solid state, which prevents rapid diffusion of the nongaseous reagents, there is the high yield conversion to the peroxomanganese(IV) **3**. Moreover, treatment of **2** and O_2 (layered above the solution) in CH_3CH_2CN at $-80\text{ }^\circ\text{C}$ results in an isolation of **3** (Figure S12) that is similar to oxygenation of **2** in the solid state. This can be attributed to the solubility/diffusion rate of the intermediate being decreased in $EtCN$ at lower temperature. It is also noted that most of mononuclear **2** are converted into the Mn(IV)- O_2 species without a detectable intermediate upon reaction of **2** in $EtCN$ at $-80\text{ }^\circ\text{C}$.

Analysis by cyclic voltammetry of CV's responses of **1** and **2** suggests that both complexes can be oxidized by O_2 . In contrast to **2**, solid-state oxidation of **1** with O_2 does not generate Mn(IV)-peroxo **3** as evidenced by the absence a ν_{OO} band at 903 cm^{-1} in ATR-FTIR spectroscopy (Scheme 4; Figure S13). Orange-red microcrystals of **1** gradually convert to a yellow-brown solid upon contacting with excess amounts of dry O_2 at ambient temperature for 2 h (Figure S14). The yellow-brown species can dissolve in THF and has a featureless UV-vis spectrum at wavelengths above 500 nm. Attempts to isolate this adduct have been unsuccessful.

As shown in Figure 10, treatment of CH_3CN solution of **1** with excess amounts of O_2 at ambient temperature also produces mixed products, **3** and **4** based on UV-vis

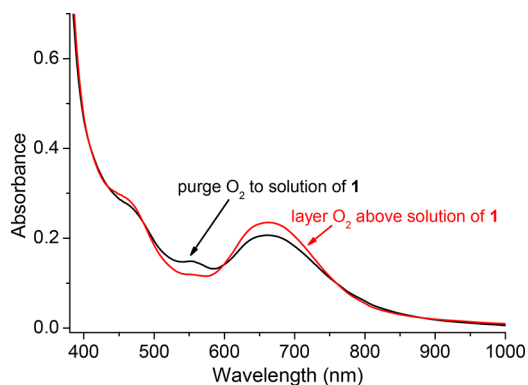


Figure 10. Comparisons of UV-vis spectra between purging O_2 into and layering O_2 above CH_3CN solution of **1** (0.16 mM).

spectroscopy. Compared to the oxidation of solution **2** with O₂ (Figure 9), the ratio between the generated **3** and **4** in this reaction is less dependent upon the oxygen addition method (Figure S15). The formation of **3** in oxidation of CH₃CN solution of **1** with O₂ is observed; however, as indicated in solid-to-solid oxygenation of **1** (Figure S13), none can evolve into **3**. Presumably, the dissociation of binuclear **1** to mononuclear solvent-bound [Mn^{II}(^{TMS}PS3)(NCCH₃)]⁻ occurs in CH₃CN solution (Scheme 4). Like oxygenation of mononuclear **2**, solvent-bound [Mn^{II}(^{TMS}PS3)(NCCH₃)]⁻ can react with O₂ to yield mononuclear **3**, and then the generated **3** can react with **1** to produce dinuclear **4** (Scheme 3). The second hypothesis for formation of **4** in this reaction may involve direct insertion of O₂ into two coordinate-unsaturated Mn(II) centers of **1**, resulting in the formation of intermediate **A**. As indicated in Scheme 3, intermediate **A** may undergo homolytic O–O bond cleavage and the generated Mn–oxo species reacts rapidly with **1** to form dimeric **4** (via a comproportionation reaction).²¹ The ESI-MS of **1** in CH₃CN shows some oxygenated fragments in which the *m/z* at 658.0 is complex **3** ([Mn(^{TMS}PS3)(O₂)]⁻ (**3**), *m/z* = 658.1 (calcd); Figure S5).⁷² However, the factors for **4** being generated preferentially and independent of the oxygen addition method in this reaction are not clear.

CONCLUSION

We describe a thiolate-bridged binuclear complex [PPN]₂[(Mn^{II}(^{TMS}PS3))₂] (**1**) which converts to the mononuclear complex [PPN][Mn^{II}(^{TMS}PS3)(DABCO)] (**2**) in the presence of excess amounts of DABCO. The activation parameters obtained from studies of variable-temperature UV–vis spectroscopy are consistent with an equilibrium in which mononuclear **2** is favored at low temperature. The CVs of **1** and **2** reveal anodic peak(s) for Mn^{III}/Mn^{II} redox couple at much negative potentials against Fc/Fc⁺, indicating rich oxidative chemistry with O₂ and other oxidants. Oxidative reactions are first examined with a Mn(IV)–peroxo **3**, leading to the formation of an unsupported oxo-bridged Mn(III) dimer **4**. The generation of **4** is proposed via a peroxo-bridged dimanganese(III) intermediate in which the O–O bond is much weaker and more readily undergoes O–O bond cleavage than that of **3**. Although the intermediate is not detected in this case, even at low temperature, a well-characterized peroxo-bridged Mn(III) dimer has been reported recently.

The cyclic voltammetry of **2** under inert atmosphere shows a reversible Mn^{III}/Mn^{II} redox couple which indicates that a stable mononuclear Mn(III) [Mn(^{TMS}PS3)(DABCO)] can be electrochemically generated.⁷³ Chemically, oxidation of **2** with O₂ in both solution and the solid state generates a mononuclear Mn(IV)–peroxo **3**. Factors which allow for the isolation of **3** may include a redox noninnocent ^{TMS}PS3³⁻ which stabilizes a formally high-valent Mn(IV) species.

The O₂ activation mediated by **1** and **2** is investigated in both solution and the solid state. Since the movement of ions is restricted in the solid state, Mn(IV)–peroxo **3** generated from reaction of mononuclear Mn(II) **2** and gas O₂ is not further oxidized by another **2** to form oxo-bridged Mn(III) dimer **4**. In solution, however, the diffusion rate of ions is fast enough and mixed products are isolated. Significantly, the oxygenation of **1** or **2** does not lead to the oxidation of thiolate donors. This is attributed to the rigidity of multidentate chelating ^{TMS}PS3³⁻ ligand. Further studies seek to characterize the intermediate

species upon oxidation of these thiolate-ligated-manganese complexes.

EXPERIMENTAL SECTION

General Procedures. Manipulations and reactions are conducted under a pure nitrogen atmosphere according to Schlenk techniques or in a glovebox (nitrogen atmosphere). Solvents are purified and distilled under nitrogen by utilizing appropriate reagents (diethyl ether from CaH₂; acetonitrile from CaH₂–P₂O₅; methylene chloride from CaH₂; hexane and tetrahydrofuran (THF) from sodium benzophenone) and stored in dried, N₂-filled flasks over 4 Å molecular sieves. The reagent ¹⁸O₂ (99 atom % ¹⁸O, Sure-Pac from Aldrich) is used as received. 2,2',2''-Trimercapto-3,3',3''-tris(trimethylsilyl)-triphenylphosphine ligand (^{TMS}PS3H₃) is synthesized according to published procedures. Li₃[^{TMS}PS3] is prepared from reaction of ^{TMS}PS3H₃ and *n*-butyllithium (2.5 M in hexane) at –20 °C. Infrared spectra (IR) are recorded either on a SHIMADZU FTIR-8400S with sealed solution cells (0.1 mm, KBr windows) or on an ATR (attenuated total reflectance)-FTIR (PerkinElmer, Frontier). UV–vis spectra are recorded on a SCINCO S-4100 or on an Agilent 8454 spectrophotometer equipped with a UNICOKU liquid N₂ cryostat. NMR spectra are obtained on an Agilent 400-MR DD2. GC–MS (an Agilent 7890A gas chromatograph connected with an Agilent 5975C mass selective detector) is used to detect the organic products. Analyses of carbon, hydrogen, and nitrogen are obtained with a CHN analyzer (Heraeus).

Physical Measurements. Electrochemical measurements are recorded on a CH Instruments 630C electrochemical potentiostat using a gas-tight three-electrode cell under N₂ at room temperature. A glassy carbon electrode (3 mm in diameter) and a platinum wire are used as working and counter electrode, respectively. Reference electrode is a nonaqueous Ag/Ag⁺ electrode. All potentials are reported against ferrocene/ferrocenium (Fc/Fc⁺). The magnetic data of the microcrystalline samples of **1**, **2**, and **4** are recorded on a SQUID magnetometer (SQUID-VSM, Quantum Design) under an external magnetic field (0.2 T) in the temperature range of 2–300 K. The magnetic susceptibility data are corrected with ligands' diamagnetism by the tabulated Pascal's constants and the sample holder.⁷⁴ The X-band EPR measurements are recorded at 77 K on a Bruker E580 CW/Pulse EPR. The X-ray single crystal crystallographic data collections for **1**, **2**, and **4** are carried out at 150 K with a Bruker SMART APEX CCD four-circle diffractometer with graphite-monochromated Mo K α radiation (λ = 0.71073 Å) outfitted with a low-temperature, nitrogen-stream aperture. The structures are solved by direct methods, in conjunction with standard difference Fourier techniques and refined by full-matrix least-squares procedures. A summary of the crystallographic parameters for the complexes **1**, **2**, and **4** is shown in Table S1. An empirical absorption correction (multiscan) is applied to the diffraction data for all structures. All non-hydrogen atoms are refined anisotropically, and all hydrogen atoms are placed in geometrically calculated positions by the riding model. All software used for diffraction data processing and crystal structure solution and refinement are contained in the SHELXL-97 program suites.

Preparation of [PPN]₂[(Mn^{II}(^{TMS}PS3))₂] (1**).** A THF/CH₃CN solution of Li₃[^{TMS}PS3] (9:1 v/v; 5 mL, 0.1 M) is added to a suspended CH₃CN solution (2 mL) containing MnCl₂ (0.063 g, 0.50 mmol) and PPNCl (0.288 g, 0.50 mmol) by syringe under N₂. The reaction mixture is stirred for 30 min at ambient temperature. The resulting orange-red solution is reduced under vacuum, and diethyl ether (50 mL) is added to precipitate the orange-red solid [PPN]₂[(Mn^{II}(^{TMS}PS3))₂] (**1**) (1.110 g, 95%). Diffusion of diethyl ether into a THF/CH₃CN (3:1 v/v) solution of **1** at –20 °C leads to red crystals suitable for X-ray crystallography. UV–vis THF/CH₃CN, 1:1 v/v): λ_{\max} (ϵ , M⁻¹ cm⁻¹) = 420 nm (650, sh). Magnetic susceptibility (solid state, 2–300 K, antiferromagnetically coupled): calcd for $g = 1.991(9)$, $2J = -57.0(5)$ cm⁻¹. ESI-MS: [(Mn(^{TMS}PS3))₂]⁻, expected *m/z* for C₅₄H₇₂P₂S₆Si₆Mn₂ = 1252.1, found *m/z* = 1252.2.

Preparation of [PPN][Mn^{II}(^{TMS}PS3)(DABCO)] (2). A THF/CH₃CN solution (3:1 v/v, 20 mL) of **1** (0.466 g, 0.20 mmol) is added to a THF solution of DABCO (20 mL, 1 M) by syringe under N₂. The reaction mixture is stirred for 10 min at ambient temperature. The resulting purple solution is reduced to 10 mL under vacuum, and a diethyl ether solution of DABCO (30 mL, 0.2 M) is added to precipitate the purple solid [PPN][Mn^{II}(^{TMS}PS3)(DABCO)] (**2**) (0.460 g, 90%). Crystals of **2** suitable for X-ray crystallography are grown by slowly adding the diethyl ether solution of DABCO (5 mL, 1 M) to layer above the CH₃CN solution of **2** (2 mL, 0.05 M) at -20 °C under N₂ for 1 week. UV-vis (CH₃CN): λ_{max} (ε, M⁻¹ cm⁻¹) = 370 (2450, sh), 535 nm (540). Magnetic susceptibility (solid state, 300 K): 5.71 μ_B. EPR spectrum (CH₃CN glass): g_⊥ = 5.21 and g_{||} = 1.95. Peaks of *m/z* for **2** ([Mn(^{TMS}PS3)(DABCO)]⁻), expected *m/z* for C₃₃H₄₈PS₃Si₃Mn = 738.1) are not able to be detected by ESI-MS, presumably because of oxygenation of **2** with air during injection of sample into the instrument (Figure S17).

Equilibrium Constant Measurement. In a glovebox (N₂ atmosphere), solids of **1** (0.029 g, 0.013 mmol) are mixed with excess amounts of DABCO (0.035 g, 0.32 mmol) in 25 mL of CH₃CN. The values for [1]₀ and [DABCO]₀ are 0.50 and 12.5 mM, respectively, where [1]₀ and [DABCO]₀ are initial concentrations for **1** and DABCO. Other sets of concentrations for [1]₀ and [DABCO]₀ (0.67 and 13.4, or 0.60 and 13.8 mM, respectively) are also prepared for equilibrium constant measurement. The mixture is then loaded into a 4 mL UV cell. The equilibrium concentration of **2** ([2]) at 25 °C can be determined from the absorption band at 535 nm (ε = 540) where the ε values for **1** and DABCO are minor contributors. According to eq 1, the equilibrium constant (K_{eq} = 9(1), the mean value is obtained from three measurements) is expressed as eq 3,

$$K_{\text{eq}} = \frac{[2]^2}{\left([1]_0 - \frac{[2]}{2}\right)\left([DABCO]_0 - [2]\right)^2} \quad (3)$$

The temperature dependence of K_{eq} (25, 15, 5, -5, -15 and -25 °C) for the same UV cell is recorded on an Agilent 8454 spectrophotometer equipped with a UNICOKU liquid N₂ cryostat. The van't Hoff equation is used to calculate ΔH° and ΔS°. The average value for ΔH° is -16(1) kJ mol⁻¹ (-16, -16, and -17) and for ΔS° is -37(2) J K⁻¹ mol⁻¹ (-39, -36, and -35). In comparison, the changes of UV-vis spectra of **1** (0.50 mM) without addition of DABCO and **1** (0.50 mM) with excess amounts of DABCO (100 equiv) are also examined in the temperature range from 25 to -25 °C, respectively. The intensities at 535 nm of individual spectra of **1** and **2** (suggesting 100% conversion from **1** with excess amounts of DABCO) show minor temperature dependence in the temperature range from 25 to -25 °C (Figure S18).

Preparation of [PPN]₂[(Mn^{III}(^{TMS}PS3)₂(μ-O)] (4). *Method A: Reaction of 2 with [PPN][Mn^{IV}(O₂)(^{TMS}PS3)] (3).*⁵⁵ A CH₃CN solution (10 mL) of **3** (0.120 g, 0.10 mmol) is added to a THF/CH₃CN solution (1:1 v/v, 30 mL) containing **2** (0.383 g, 0.30 mmol) and DABCO (1.680 g, 15 mmol) by syringe under N₂. The reaction mixture is stirred for 30 min at ambient temperature. Analysis of the dark-green solution by UV-vis spectroscopy reveals the formation of **4**. Diethyl ether is added to precipitate the dark-green solid, [PPN]₂[(Mn^{III}(^{TMS}PS3)₂(μ-O)] (**4**; 0.446 g, 95%). Diffusion of diethyl ether into a CH₃CN solution of **4** at -20 °C leads to dark-green crystals suitable for X-ray crystallography. UV-vis (CH₃CN): λ_{max} (ε, M⁻¹ cm⁻¹) = 450 (5410), 670 nm (3760). Magnetic susceptibility (solid state, 100–300 K, antiferromagnetically coupled): calcd for g = 2.01(3), 2J = -152(3) cm⁻¹. ESI-MS: [(Mn(^{TMS}PS3)₂(μ-O)]⁻, expected *m/z* for C₅₄H₇₂O₁P₂S₆Si₆Mn₂ = 1268.1, found *m/z* = 1268.2. Anal. Calcd for C₁₂₆H₁₃₂N₂O₆S₆Si₆Mn₂: C, 64.48; H, 5.67; N, 1.19. Found: C, 64.30; H, 5.79; N, 1.37.

*Method B: Reaction of 1 with [PPN][Mn^{IV}(O₂)(^{TMS}PS3)] (3).*⁵⁵ A CH₃CN solution (5 mL) of **3** (0.08 g, 0.067 mmol) is added to a CH₃CN solution (10 mL) of **1** (0.233 g, 0.10 mmol) by syringe under N₂. The reaction mixture is stirred for 30 min at ambient temperature. The resulting dark-green solution is reduced to 5 mL under vacuum,

and diethyl ether (30 mL) is added to precipitate the dark-green solid [PPN]₂[(Mn^{III}(^{TMS}PS3)₂(μ-O)] (**4**) (0.220 g, 70%).

Method C: Reaction of 2 with Iodosylbenzene (PhIO). A suspended CH₃CN solution (10 mL) of PhIO (0.035 g, 0.16 mmol) is added to a THF/CH₃CN solution (1:1 v/v, 30 mL) containing **2** (0.383 g, 0.3 mmol) and DABCO (1.68 g, 15 mmol) by syringe under N₂. The reaction mixture is stirred for 60 min at ambient temperature under N₂. Analysis of the dark-green solution by UV-vis spectroscopy reveals the formation of **4**. Diethyl ether is added to precipitate the dark-green solid, **4** (0.450 g, 96%).

Reaction of 1 with Dioxygen in the Solid State. Orange-red microcrystals of **1** (0.055 g, 0.020 mmol) are placed in a vial and then exposed to air or dry O₂ for 2 h. During this period, a color change of microcrystals of **1** is observed from orange-red to yellow-brown. IR (solid, cm⁻¹): 3060(w), 2950(w), 2890(w), 1588(w), 1554(w), 1532(w), 1482(w), 1438(m), 1350(m), 1238(m), 1192(w), 1114(m), 1044(w), 998(w), 848(s), 830(s), 799(w), 781(w), 750(m), 722(s), 690(s). The UV-vis spectrum of the yellow-brown species (THF) is featureless above 500 nm. Characterization of this species was unsuccessful.

Reaction of 1 with Dioxygen in Solution. Oxygen gas (excess) is purged through a CH₃CN (25 mL) solution of **1** (0.130 g, 0.050 mmol) at ambient temperature for 30 min. A change of color from orange-red to dark-green is observed. Calculations from UV-vis spectral deconvolution reveal the formation of **3** (24% yield based on ε at 550 nm) and **4** (50% yield based on ε at 670 nm), respectively. When excess amounts of O₂ are slowly added to layer above the mixture containing **1** (0.130 g, 0.050 mmol) at ambient temperature for 30 min, the color of solution changes from orange-red to green. Analysis of UV-vis spectra obtained that the yields of **3** and **4** are 12% and 68%, respectively.

Reaction of 2 with Dioxygen in the Solid State. Purple microcrystals of **2** (0.064 g, 0.050 mmol) are loaded into a vial and then exposed to air or excess amounts of dry ¹⁶O₂ or ¹⁸O₂ for 2 h. During this period, a color change of microcrystals of **2** is observed from purple to dark-purple. The reaction mixture is then kept under vacuum to remove the remaining ¹⁶O₂ or ¹⁸O₂ and is sent to a glovebox (O₂ < 0.5 ppm, H₂O < 0.5 ppm). A weak peak at 903 cm⁻¹ (ν_{OO}) observed by FTIR (KBr, 861 cm⁻¹ for using ¹⁸O₂) and three absorption bands at 490, 550, and 755 nm (dissolved in CH₃CN under N₂ in the glovebox) in the UV-vis spectroscopy confirm the formation of **3** (95% yield based on ε at 550 nm). In comparison, microcrystals of **2** are dissolved in CH₃CN under N₂ in the glovebox. None of the three absorption bands at 490, 550, and 755 nm are observed by UV-vis spectroscopy.

Reaction of 2 with Dioxygen in Solution. Oxygen gas (excess) is purged through a CH₃CN (25 mL) solution containing **2** (0.064 g, 0.050 mmol) and DABCO (0.28 g, 2.5 mmol) at ambient temperature for 10 min. A change of color from purple to red-purple is observed. Calculations from UV-vis spectral deconvolution reveal the formation of **3** (63% yield based on ε at 550 nm) and **4** (8% yield based on ε at 670 nm), respectively. When excess amounts of O₂ are slowly added to layer above the mixture containing **2** (0.064 g, 0.050 mmol) and DABCO (0.28 g, 2.5 mmol) at ambient temperature for 30 min, the color of solution changes from purple to brown. Analysis of UV-vis spectra obtained that the yields of **3** and **4** are 37% and 25%, respectively.

■ ASSOCIATED CONTENT

📄 Supporting Information

The Supporting Information is available free of charge on the ACS Publications website at DOI: 10.1021/acs.inorgchem.7b01513.

UV-vis, FTIR, ESI-MS, EPR, SQUID, and powder X-ray diffraction data, ab initio calculations, and crystallographic parameters (PDF)

Accession Codes

CCDC 1556237–1556239 and 1563888 contain the supplementary crystallographic data for this paper. These data can be obtained free of charge via www.ccdc.cam.ac.uk/data_request/cif, or by emailing data_request@ccdc.cam.ac.uk, or by contacting The Cambridge Crystallographic Data Centre, 12 Union Road, Cambridge CB2 1EZ, UK; fax: +44 1223 336033.

AUTHOR INFORMATION

Corresponding Authors

*E-mail: cmlee@nttu.edu.tw.

*E-mail: mhchiang@chem.sinica.edu.tw.

*E-mail: Scott.Bohle@mcgill.ca.

ORCID

Chien-Ming Lee: 0000-0001-8529-4279

Ming-Hsi Chiang: 0000-0002-7632-9369

D. Scott Bohle: 0000-0001-5833-5696

Notes

The authors declare no competing financial interest.

ACKNOWLEDGMENTS

C.-M.L. thanks Dr. Lai-Chin Wu (National Synchrotron Radiation Research Center, Taiwan) for collection of powder X-ray diffraction data and is thankful for the support from the Ministry of Science and Technology of Taiwan (Grant 105-2113-M-143-001).

REFERENCES

- (1) VanAtta, R. B.; Strouse, C. E.; Hanson, L. K.; Valentine, J. S. [Peroxo-tetraphenylporphinato]manganese(III) and [Chlorotetraphenylporphinato]manganese(II) Anions. Syntheses, Crystal Structures, and Electronic Structures. *J. Am. Chem. Soc.* **1987**, *109*, 1425–1434.
- (2) Bossek, U.; Weyhermueller, T.; Wieghardt, K.; Nuber, B.; Weiss, J. $[L_2Mn_2(\mu-O)_2(\mu-O_2)](ClO_4)_2$: The First Binuclear(μ -Peroxo)-dimanganese(IV) Complex ($L = 1,4,7$ -Trimethyl-1,4,7-triazacyclononane). A Model for the $S_4 \rightarrow S_0$ Transformation in the Oxygen-Evolving Complex in Photosynthesis. *J. Am. Chem. Soc.* **1990**, *112*, 6387–6388.
- (3) Kitajima, N.; Komatsuzaki, H.; Hikichi, S.; Osawa, M.; Moro-oka, Y. A Monomeric Side-On Peroxo Manganese(III) Complex: $Mn(O_2)-(3,5-iPr_2pzH)(HB(3,5-iPr_2pz)_3)$. *J. Am. Chem. Soc.* **1994**, *116*, 11596–11597.
- (4) Seo, M. S.; Kim, J. Y.; Annaraj, J.; Kim, Y.; Lee, Y.-M.; Kim, S.-J.; Kim, J.; Nam, W. $[Mn(tmc)(O_2)]^+$: A Side-On Peroxido Manganese(III) Complex Bearing a Non-Heme Ligand. *Angew. Chem., Int. Ed.* **2007**, *46*, 377–380.
- (5) Shook, R. L.; Gunderson, W. A.; Greaves, J.; Ziller, J. W.; Hendrich, M. P.; Borovik, A. S. A Monomeric Mn^{III} -Peroxo Complex Derived Directly from Dioxygen. *J. Am. Chem. Soc.* **2008**, *130*, 8888–8889.
- (6) Annaraj, J.; Cho, J.; Lee, Y.-M.; Kim, S. Y.; Latifi, R.; Visser, S. P. d.; Nam, W. Structural Characterization and Remarkable Axial Ligand Effect on the Nucleophilic Reactivity of a Nonheme Manganese(III)-Peroxo Complex. *Angew. Chem., Int. Ed.* **2009**, *48*, 4150–4153.
- (7) Kim, S. H.; Park, H.; Seo, M. S.; Kubo, M.; Ogura, T.; Klajn, J.; Gryko, D. T.; Valentine, J. S.; Nam, W. Reversible O–O Bond Cleavage and Formation between Mn(IV)-Peroxo and Mn(V)-Oxo Corroles. *J. Am. Chem. Soc.* **2010**, *132*, 14030–14032.
- (8) Geiger, R. A.; Chattopadhyay, S.; Day, V. W.; Jackson, T. A. A Series of Peroxomanganese(III) Complexes Supported by Tetradentate Aminopyridyl Ligands: Detailed Spectroscopic and Computational Studies. *J. Am. Chem. Soc.* **2010**, *132*, 2821–2831.
- (9) Shook, R. L.; Borovik, A. S. Role of the Secondary Coordination Sphere in Metal-Mediated Dioxygen Activation. *Inorg. Chem.* **2010**, *49*, 3646–3660.
- (10) Shook, R. L.; Peterson, S.; Greaves, J.; Moore, C.; Rheingold, A. L.; Borovik, A. S. Catalytic Reduction of Dioxygen to Water with a Monomeric Manganese Complex at Room Temperature. *J. Am. Chem. Soc.* **2011**, *133*, 5810–5817.
- (11) Coggins, M. K.; Kovacs, J. A. Structural and Spectroscopic Characterization of Metastable Thiolate-Ligated Manganese(III) Alkylperoxy Species. *J. Am. Chem. Soc.* **2011**, *133*, 12470–12473.
- (12) Coggins, M. K.; Toledo, S.; Shaffer, E.; Kaminsky, W.; Shearer, J.; Kovacs, J. A. Characterization and Dioxygen Reactivity of a New Series of Coordinatively Unsaturated Thiolate-Ligated Manganese(II) Complexes. *Inorg. Chem.* **2012**, *51*, 6633–6644.
- (13) Coggins, M. K.; Martin-Diaconescu, V.; DeBeer, S.; Kovacs, J. A. Correlation Between Structural, Spectroscopic, and Reactivity Properties Within a Series of Structurally Analogous Metastable Manganese(III)-Alkylperoxy Complexes. *J. Am. Chem. Soc.* **2013**, *135*, 4260–4272.
- (14) Coggins, M. K.; Sun, X.; Kwak, Y.; Solomon, E. I.; Rybak-Akimova, E.; Kovacs, J. A. Characterization of Metastable Intermediates Formed in the Reaction between a Mn(II) Complex and Dioxygen, Including a Crystallographic Structure of a Binuclear Mn(III)-Peroxo Species. *J. Am. Chem. Soc.* **2013**, *135*, 5631–5640.
- (15) Ghachtouli, S. E.; Ching, H. Y. V.; Lassalle-Kaiser, B.; Guillot, R.; Leto, D. F.; Chattopadhyay, S.; Jackson, T. A.; Dorlet, P.; Anxolabéhère-Mallart, E. Electrochemical formation of Mn^{III} -peroxy complexes supported by pentadentate amino pyridine and imidazole ligands. *Chem. Commun.* **2013**, *49*, 5696–5698.
- (16) Kovacs, J. A. Tuning the Relative Stability and Reactivity of Manganese Dioxygen and Peroxo Intermediates via Systematic Ligand Modification. *Acc. Chem. Res.* **2015**, *48*, 2744–2753.
- (17) Rees, J. A.; Martin-Diaconescu, V.; Kovacs, J. A.; DeBeer, S. X-ray Absorption and Emission Study of Dioxygen Activation by a Small-Molecule Manganese Complex. *Inorg. Chem.* **2015**, *54*, 6410–6422.
- (18) Gennari, M.; Brazzolotto, D.; Pécaut, J.; Cherrier, M. V.; Pollock, C. J.; DeBeer, S.; Retegan, M.; Pantazis, D. A.; Neese, F.; Rouzières, M.; Clérac, R.; Duboc, C. Dioxygen Activation and Catalytic Reduction to Hydrogen Peroxide by a Thiolate-Bridged Dimanganese(II) Complex with a Pendant Thiol. *J. Am. Chem. Soc.* **2015**, *137*, 8644–8653.
- (19) Deville, C.; Padamati, S. K.; Sundberg, J.; McKee, V.; Browne, W. R.; McKenzie, C. J. O_2 Activation and Double C–H Oxidation by a Mononuclear Manganese(II) Complex. *Angew. Chem., Int. Ed.* **2016**, *55*, 545–549.
- (20) Hong, S.; Lee, Y.-M.; Sankaralingam, M.; Vardhaman, A. K.; Park, Y. J.; Cho, K.-B.; Ogura, T.; Sarangi, R.; Fukuzumi, S.; Nam, W. A Manganese(V)-Oxo Complex: Synthesis by Dioxygen Activation and Enhancement of Its Oxidizing Power by Binding Scandium Ion. *J. Am. Chem. Soc.* **2016**, *138*, 8523–8532.
- (21) Brazzolotto, D.; Reinhard, F. G. C.; Smith-Jones, J.; Retegan, M.; Amidani, L.; Faponle, A. S.; Ray, K.; Philouze, C.; Visser, S. P. d.; Gennari, M.; Duboc, C. A High-Valent Non-Heme μ -Oxo Manganese(IV) Dimer Generated from a Thiolate-Bound Manganese(II) Complex and Dioxygen. *Angew. Chem., Int. Ed.* **2017**, *56*, 8211–8215.
- (22) Vetting, M. W.; Wackett, L. P.; Que, L., Jr.; Lipscomb, J. D.; Ohlendorf, D. H. Crystallographic Comparison of Manganese- and Iron-Dependent Homoproteocatechuate 2,3-Dioxygenases. *J. Bacteriol.* **2004**, *186*, 1945–1958.
- (23) Gunderson, W. A.; Zatsman, A. I.; Emerson, J. P.; Farquhar, E. R.; Que, L., Jr.; Lipscomb, J. D.; Hendrich, M. P. Electron Paramagnetic Resonance Detection of Intermediates in the Enzymatic Cycle of an Extradiol Dioxygenase. *J. Am. Chem. Soc.* **2008**, *130*, 14465–14467.
- (24) Boal, A. K.; Cotruvo, J. A., Jr.; Stubbe, J.; Rosenzweig, A. C. Structural Basis for Activation of Class Ib Ribonucleotide Reductase. *Science* **2010**, *329*, 1526–1530.
- (25) Cotruvo, J. A., Jr.; Stich, T. A.; Britt, R. D.; Stubbe, J. Mechanism of Assembly of the Dimanganese-Tyrosyl Radical Cofactor

- of Class Ib Ribonucleotide Reductase: Enzymatic Generation of Superoxide Is Required for Tyrosine Oxidation via a Mn(III)Mn(IV) Intermediate. *J. Am. Chem. Soc.* **2013**, *135*, 4027–4039.
- (26) Miller, A.-F. Superoxide dismutases: active sites that save, but a protein that kills. *Curr. Opin. Chem. Biol.* **2004**, *8*, 162–168.
- (27) Sheng, Y.; Abreu, I. A.; Cabelli, D. E.; Maroney, M. J.; Miller, A.-F.; Teixeira, M.; Valentine, J. S. Superoxide Dismutases and Superoxide Reductases. *Chem. Rev.* **2014**, *114*, 3854–3918.
- (28) Wu, A. J.; Penner-Hahn, J. E.; Pecoraro, V. L. Structural, Spectroscopic, and Reactivity Models for the Manganese Catalases. *Chem. Rev.* **2004**, *104*, 903–938.
- (29) Christianson, D. W. Structural Chemistry and Biology of Manganese Metalloenzymes. *Prog. Biophys. Mol. Biol.* **1997**, *67*, 217–252.
- (30) Yano, J.; Yachandra, V. Mn₄Ca Cluster in Photosynthesis: Where and How Water is Oxidized to Dioxygen. *Chem. Rev.* **2014**, *114*, 4175–4205.
- (31) Suga, M.; Akita, F.; Hirata, K.; Ueno, G.; Murakami, H.; Nakajima, Y.; Shimizu, T.; Yamashita, K.; Yamamoto, M.; Ago, H.; Shen, J.-R. Native structure of photosystem II at 1.95 Å resolution viewed by femtosecond X-ray pulses. *Nature* **2015**, *517*, 99–103.
- (32) Young, K. J.; Brennan, B. J.; Tagore, R.; Brudvig, G. W. Photosynthetic Water Oxidation: Insights from Manganese Model Chemistry. *Acc. Chem. Res.* **2015**, *48*, 567–574.
- (33) Cotruvo, J. A., Jr.; Stubbe, J. An Active Dimanganese(III)-Tyrosyl Radical Cofactor in *Escherichia coli* Class Ib Ribonucleotide Reductase. *Biochemistry* **2010**, *49*, 1297–1309.
- (34) Zhang, Y.; Stubbe, J. *Bacillus subtilis* Class Ib Ribonucleotide Reductase Is a Dimanganese(III)-Tyrosyl Radical Enzyme. *Biochemistry* **2011**, *50*, 5615–5623.
- (35) Hage, R.; Lienke, A. Applications of Transition-Metal Catalysts to Textile and Wood-Pulp Bleaching. *Angew. Chem., Int. Ed.* **2006**, *45*, 206–222.
- (36) Sibbons, K. F.; Shastri, K.; Watkinson, M. The application of manganese complexes of ligands derived from 1,4,7-triazacyclononane in oxidative catalysis. *Dalton Trans.* **2006**, 645–661.
- (37) Neu, H. M.; Baglia, R. A.; Goldberg, D. P. A Balancing Act: Stability versus Reactivity of Mn(O) Complexes. *Acc. Chem. Res.* **2015**, *48*, 2754–2764.
- (38) Cho, J.; Sarangi, R.; Nam, W. Mononuclear Metal O₂ Complexes Bearing Macrocyclic N-Tetramethylated Cyclam Ligands. *Acc. Chem. Res.* **2012**, *45*, 1321–1330.
- (39) Sahu, S.; Goldberg, D. P. Activation of Dioxygen by Iron and Manganese Complexes: A Heme and Nonheme Perspective. *J. Am. Chem. Soc.* **2016**, *138*, 11410–11428.
- (40) Ray, K.; Pfaff, F. F.; Wang, B.; Nam, W. Status of Reactive Non-Heme Metal–Oxygen Intermediates in Chemical and Enzymatic Reactions. *J. Am. Chem. Soc.* **2014**, *136*, 13942–13958.
- (41) Balch, A. L.; Chan, Y.-W.; Cheng, R.-J.; La Mar, G. N.; Latos-Grazynski, L.; Renner, M. W. Oxygenation Patterns for Iron(II) Porphyrins. Peroxo and Ferryl(Fe^{IV}O) Intermediates Detected by ¹H Nuclear Magnetic Resonance Spectroscopy during the Oxygenation of (Tetramesitylporphyrin)iron(II). *J. Am. Chem. Soc.* **1984**, *106*, 7779–7785.
- (42) Solomon, E. I.; Heppner, D. E.; Johnston, E. M.; Ginsbach, J. W.; Cirera, J.; Qayyum, M.; Kieber-Emmons, M. T.; Kjaergaard, C. H.; Hadt, R. G.; Tian, L. Copper Active Sites in Biology. *Chem. Rev.* **2014**, *114*, 3659–3853.
- (43) Lee, J. Y.; Karlin, K. D. Elaboration of copper–oxygen mediated C–H activation chemistry in consideration of future fuel and feedstock generation. *Curr. Opin. Chem. Biol.* **2015**, *25*, 184–193.
- (44) Lewis, E. A.; Tolman, W. B. Reactivity of dioxygen–copper systems. *Chem. Rev.* **2004**, *104*, 1047–1076.
- (45) Kumar, M.; Colpas, G. J.; Day, R. O.; Maroney, M. J. Ligand Oxidation in a Nickel Thiolate Complex: A Model for the Deactivation of Hydrogenase by O₂. *J. Am. Chem. Soc.* **1989**, *111*, 8323–8325.
- (46) Grapperhaus, C. A.; Darenbourg, M. Y. Oxygen Capture by Sulfur in Nickel Thiolates. *Acc. Chem. Res.* **1998**, *31*, 451–459.
- (47) Lee, C.-M.; Hsieh, C.-H.; Dutta, A.; Lee, G.-H.; Liaw, W.-F. Oxygen Binding to Sulfur in Nitrosylated Iron-Thiolate Complexes: Relevance to the Fe-Containing Nitrile Hydratases. *J. Am. Chem. Soc.* **2003**, *125*, 11492–11493.
- (48) Jiang, Y.; Widger, L. R.; Kasper, G. D.; Siegler, M. A.; Goldberg, D. P. Iron(II)-Thiolate S-Oxygenation by O₂: Synthetic Models of Cysteine Dioxygenase. *J. Am. Chem. Soc.* **2010**, *132*, 12214–12215.
- (49) Kovacs, J. A.; Brines, L. M. Understanding How the Thiolate Sulfur Contributes to the Function of the Non-Heme Iron Enzyme Superoxide Reductase. *Acc. Chem. Res.* **2007**, *40*, 501–509.
- (50) Niemoth-Anderson, J. D.; Clark, K. A. F.; George, T. A.; Ross, C. R., II Five-Coordinate Diamagnetic Iron(IV) Complexes With A Trigonal Planar Arrangement of Thiolate Ligand Atoms: Synthesis and Crystal Structure of [FeX(PS₃)] (X = Cl, Br or I; PS₃H₃ = [P(C^{'''}H₃-3-Me₃Si-2-SH)₃]). *J. Am. Chem. Soc.* **2000**, *122*, 3977–3978.
- (51) Chang, H.-C.; Lo, F.-C.; Liu, W.-C.; Lin, T.-H.; Liaw, W.-F.; Kuo, T.-S.; Lee, W.-Z. Ambient Stable Trigonal Bipyramidal Copper(III) Complexes Equipped with an Exchangeable Axial Ligand. *Inorg. Chem.* **2015**, *54*, 5527–5533.
- (52) Chiou, T.-W.; Tseng, Y.-M.; Lu, T.-T.; Weng, T.-C.; Sokaras, D.; Ho, W.-C.; Kuo, T.-S.; Jang, L.-Y.; Lee, J.-F.; Liaw, W.-F. [Ni^{III}(OMe)]-mediated reductive activation of CO₂ affording a Ni(κ¹-OCO) complex. *Chem. Sci.* **2016**, *7*, 3640–3644.
- (53) Hsu, H.-F.; Chu, W.-C.; Hung, C.-H.; Liao, J.-H. The First Example of a Seven-Coordinate Vanadium(III) Thiolate Complex Containing the Hydrazine Molecule, an Intermediate of Nitrogen Fixation. *Inorg. Chem.* **2003**, *42*, 7369–7371.
- (54) Lee, C.-M.; Chen, C.-H.; Liao, F.-X.; Hu, C.-H.; Lee, G.-H. Mononuclear Ni^{III}-Alkyl Complexes (Alkyl = Me and Et): Relevance to the Acetyl-CoA Synthase and Methyl-CoM Reductase. *J. Am. Chem. Soc.* **2010**, *132*, 9256–9258.
- (55) Lee, C.-M.; Chuo, C.-H.; Chen, C.-H.; Hu, C.-C.; Chiang, M.-H.; Tseng, Y.-J.; Hu, C.-H.; Lee, G.-H. Structural and Spectroscopic Characterization of a Monomeric Side-On Manganese(IV) Peroxo Complex. *Angew. Chem., Int. Ed.* **2012**, *51*, 5427–5430.
- (56) Cady, C. W.; Crabtree, R. H.; Brudvig, G. W. Functional models for the oxygen-evolving complex of photosystem II. *Coord. Chem. Rev.* **2008**, *252*, 444–455.
- (57) Vogt, L. H., Jr.; Zalkin, A.; Templeton, D. H. The Crystal and Molecular Structure of Phthalocyanatopyridinemanganese(III)-μ-oxo-phthalocyanatopyridinemanganese(III) Dipyridinate. *Inorg. Chem.* **1967**, *6*, 1725–1730.
- (58) Ghosh, K.; Eroy-Reveles, A. A.; Olmstead, M. M.; Mascharak, P. K. Reductive Nitrosylation and Proton-Assisted Bridge Splitting of a (μ-Oxo)dimanganese(III) Complex Derived from a Polypyridine Ligand with One Carboxamide Group. *Inorg. Chem.* **2005**, *44*, 8469–8475.
- (59) Baffert, C.; Collomb, M.-N.; Deronzier, A.; Pécaut, J.; Limburg, J.; Crabtree, R. H.; Brudvig, G. W. Two New Terpyridine Dimanganese Complexes: A Manganese(III,III) Complex with a Single Unsupported Oxo Bridge and a Manganese(III,IV) Complex with a Dioxo Bridge. Synthesis, Structure, and Redox Properties. *Inorg. Chem.* **2002**, *41*, 1404–1411.
- (60) Triller, M. U.; Hsieh, W.-Y.; Pecoraro, V. L.; Rompel, A.; Krebs, B. Preparation of Highly Efficient Manganese Catalase Mimics. *Inorg. Chem.* **2002**, *41*, 5544–5554.
- (61) Horner, O.; Anxolabéhère-Mallart, E.; Charlot, M.-F.; Tchertanov, L.; Guilhem, J.; Mattioli, T. A.; Boussac, A.; Girerd, J.-J. A New Manganese Dinuclear Complex with Phenolate Ligands and a Single Unsupported Oxo Bridge. Storage of Two Positive Charges within Less than 500 mV. Relevance to Photosynthesis. *Inorg. Chem.* **1999**, *38*, 1222–1232.
- (62) Kipke, C. A.; Scott, M. J.; Gohdes, J. W.; Armstrong, W. H. Synthesis, Structure, and Magnetic Properties of a Reactive Complex Containing a Nearly Linear Mn^{III}–O–Mn^{III} Core, [Mn₂O(S-NO₂saldien)₂]. *Inorg. Chem.* **1990**, *29*, 2193–2194.
- (63) Costa, T.; Dorfman, J. R.; Hagen, K. S.; Holm, R. H. Synthesis and Stereochemistry of Mono-, Bi-, and Tetranuclear Manganese Thiolates. *Inorg. Chem.* **1983**, *22*, 4091–4099.

(64) Seela, J. L.; Knapp, M. J.; Kolack, K. S.; Chang, H.-R.; Huffman, J. C.; Hendrickson, D. N.; Christou, G. Structural and Magnetochemical Properties of Mono-, Di-, and Trinuclear Manganese(III) Dithiolate Complexes. *Inorg. Chem.* **1998**, *37*, 516–525.

(65) Cooper, S. R.; Dismukes, G. C.; Klein, M. P.; Calvin, M. Mixed Valence Interactions in Di- μ -oxo Bridged Manganese Complexes. Electron Paramagnetic Resonance and Magnetic Susceptibility Studies. *J. Am. Chem. Soc.* **1978**, *100*, 7248–7252.

(66) Blasco, S.; Cano, J.; Clares, M. P.; García-Granda, S.; Doménech, A.; Jiménez, H. R.; Verdejo, B. a.; Lloret, F.; García-España, E. A Binuclear Mn^{III} Complex of a Scorpiand-Like Ligand Displaying a Single Unsupported Mn^{III}–O–Mn^{III} Bridge. *Inorg. Chem.* **2012**, *51*, 11698–11706.

(67) Franolic, J. D.; Wang, W. Y.; Millar, M. Synthesis, Structure, and Characterization of a Mixed-Valence [Ni(II)Ni(III)] Thiolate Dimer. *J. Am. Chem. Soc.* **1992**, *114*, 6587–6588.

(68) Lee, C.-M.; Chiou, T.-W.; Chen, H.-H.; Chiang, C.-Y.; Kuo, T.-S.; Liaw, W.-F. Mononuclear Ni(II)-Thiolate Complexes with Pendant Thiol and Dinuclear Ni(III/II)-Thiolate Complexes with Ni \cdots Ni Interaction Regulated by the Oxidation Levels of Nickels and the Coordinated Ligands. *Inorg. Chem.* **2007**, *46*, 8913–8923.

(69) Hsu, H.-F.; Su, C.-L.; Gopal, N. O.; Wu, C.-C.; Chu, W.-C.; Tsai, Y.-F.; Chang, Y.-H.; Liu, Y.-H.; Kuo, T.-S.; Ke, S.-C. Redox Chemistry in the Reaction of Oxovanadium(V) with Thiolate-Containing Ligands: the Isolation and Characterization of Non-Oxo Vanadium(IV) Complexes Containing Disulfide and Thioether Groups. *Eur. J. Inorg. Chem.* **2006**, *2006*, 1161–1167.

(70) Pérez-Lourido, P.; Romero, J.; Rodríguez, L.; García-Vázquez, J. A.; Castro, J.; Sousa, A.; Dilworth, J. R.; Nascimento, O. R. Synthesis, structure and characterisation of a Mn(IV) complex with a potentially tridentate phosphinothiol ligand. *Inorg. Chem. Commun.* **2002**, *5*, 337–339.

(71) The yield of **3** is dependent on how long the solid sample of **2** is exposed with O₂. It is also noted that the conversion for the ground solid sample of **2** is faster.

(72) The oxygenated fragments may be derived from oxygenation with air during the injection of solution of **1** into the ESI-MS instrument.

(73) Chemically, oxidation of **2** (1 equiv) with ferrocenium tetrafluoroborate (1 equiv, [Fc][BF₄]) under N₂ leads to the formation of mononuclear neutral Mn(III) [Mn(^{TMS}PS3)(DABCO)] (Figure S16).

(74) Bain, G. A.; Berry, J. F. Diamagnetic Corrections and Pascal's Constants. *J. Chem. Educ.* **2008**, *85*, 532–536.